

A CATALOG OF 3MM POINT SOURCES IN THE SGR B2 CLOUD: SIGNS OF EXTENDED STAR FORMATION IN A CMZ CLOUD

ADAM GINSBURG^{1,2}

¹ *Jansky fellow of the National Radio Astronomy Observatory, Socorro, NM 87801 USA*

² *European Southern Observatory, Karl-Schwarzschild-Straße 2, D-85748 Garching bei München, Germany*

ABSTRACT

We report ALMA observations at 3 mm of the extended Sgr B2 cloud. We detected 243 compact sources, the majority of which have extents smaller than 5000 AU. These sources are predominantly protostars or centrally condensed prestellar cores. The spatial distribution of these sources demonstrates that Sgr B2 is experiencing a highly extended star formation event, not just an isolated ‘starburst’ within the protocluster regions M, N, and S. While all protostars reside in regions of high column density, not all regions of high column density contain a high density of protostars. We observe a threshold for high-mass star formation that is substantially higher than the local threshold for star formation, implying either that high-mass star formation requires a higher column density or that the star formation threshold in the CMZ is higher than locally. These observations constitute the largest single, possibly coeval, sample of forming massive stars.

This version produced Thursday 8th June, 2017 at 22:52.

1. INTRODUCTION

The Central Molecular Zone (CMZ) of our Galaxy appears to be overall deficient in star formation relative to the gas mass it contains (Longmore et al. 2013; Kauffmann et al. 2016a,b; Barnes et al. 2016, 2017). This deficiency suggests that star formation laws, i.e., the empirical relations between the star formation rate and gas density, are not universal. The gas conditions in the Galactic center provide a powerful lever arm in a few parameters (e.g., pressure, temperature, velocity dispersion Ginsburg et al. 2016; Immer et al. 2016; Shetty et al. 2012; Henshaw et al. 2016) to assess the influence of environmental effects on star formation.

The observations that have demonstrated the star formation deficiency compare bulk tracers of star formation to $\gtrsim 0.1$ pc resolution gas observations (Barnes et al. 2017, e.g.). More recently, high-resolution observations of selected clouds in the CMZ have revealed very few star-forming cores even when examined at high resolution and sensitivity (Rathborne et al. 2015; Kauffmann et al. 2016a,b). The only sites with obvious signs of ongoing star formation along the CMZ dust ridge are the Sgr B2 N, M, and S protoclusters (Schmiedeke et al. 2016) and, at a much lower level, Clouds C, D, and E (Ginsburg et al. 2015; Barnes et al. 2017, Walker et al., in prep.). These regions contain a handful of high-mass cores detected with ALMA, but only a small number of protostars.

We report the first observations of extended, ongoing star formation in a Galactic center cloud *not* isolated to a centralized protocluster dust clump. We observed a $\sim 15 \times 15$ pc section of the Sgr B2 cloud and identified star formation along the entire molecular dust ridge known as Sgr B2 Deep South (DS). These observations allow us to perform the first star-counting based determination of the star formation rate within the dense molecular gas of the CMZ.

We adopt a distance to Sgr B2 8.4 kpc, which is consistent with Sgr B2 being located in the CMZ dust ridge. While Reid et al. (2009) measure a closer distance of 7.9 kpc, we use a value closer to the IAU-recommended Galactic Center distance of 8.5 kpc, accounting for the distance difference of ≈ 100 pc measured by Reid et al. (2009).

We describe the observations in Section 2. In this paper, we focus on the continuum sources, which we identify in Section 3.1. We classify the sources in Section 3.2.

2. OBSERVATION AND DATA REDUCTION

2.1. ALMA data

Data were acquired as part of ALMA project 2013.1.00269.S. Observations were taken in ALMA Band 3 with the 12m Total Power array (not included in this work), the ALMA 7m array, and in two configurations with the ALMA 12m array. The setup included the maximum allowed number of channels, 30720, across 4 spectral windows in a single polarization; the single-polarization mode was adopted to support moderate spectral resolution across the broad bandwidth. The basebands were centered at 89.48, 91.28, 101.37, and 103.23 GHz with bandwidth 1.875 GHz.

The ALMA QA2 calibrated measurement sets were combined to make a single high-resolution, high-dynamic range data set. We imaged the continuum jointly across all four basebands, and found that the central regions surrounding Sgr B2 M were severely affected by artifacts that could not be cleaned out. We therefore ran 3 iterations of phase-only self-calibration and two iterations of amplitude + phase self-calibration, the latter using multi-scale multi-frequency synthesis with two Taylor terms, to yield a substantially improved image (see Appendix B). The total dynamic range, measured as the peak brightness in Sgr B2 to the RMS noise in a signal-free region of the combined 7m+12m image, is 18000 (noise ~ 0.09 mJy/beam, 0.05 K), while the dynamic range within one primary beam ($\sim 0.5'$) of Sgr B2M is only 5300 (noise ~ 0.3 mJy/beam, 0.16 K). Because of the dynamic range limitations and an empirical determination that clean did not converge if allowed to go too deep, we cleaned to a threshold of 0.1 mJy/beam over all pixels with $S_\nu > 2.5$ mJy bm^{-1} as determined from a previous iteration. The final image used for most of the analysis in this paper was imaged with Briggs robust parameter 0.5, achieving a beam size $0.54 \times 0.46''$.

We also produced cubes of all of the spectral lines. These were lightly cleaned with a maximum of 2000 iterations of cleaning to a threshold of 100 mJy/beam. No self-calibration was applied. Before continuum subtraction, dynamic range related artifacts similar to those in the continuum images were present, but these structures are identical across frequencies, and were therefore removable in the image domain. We use median-subtracted cubes for the majority of our analysis, noting that the only location in which an error on the median-estimated continuum $> 5\%$ is expected is the Sgr B2 North core (Sanchez-Monge et al. 2017).

The processed data are available from http://apps.canfar.net/storage/list/SgrB2_ALMA_3mm in the form of four ~ 225 GB data cubes. Additional data sets will be made available via dataverse or some other service prior to submission.

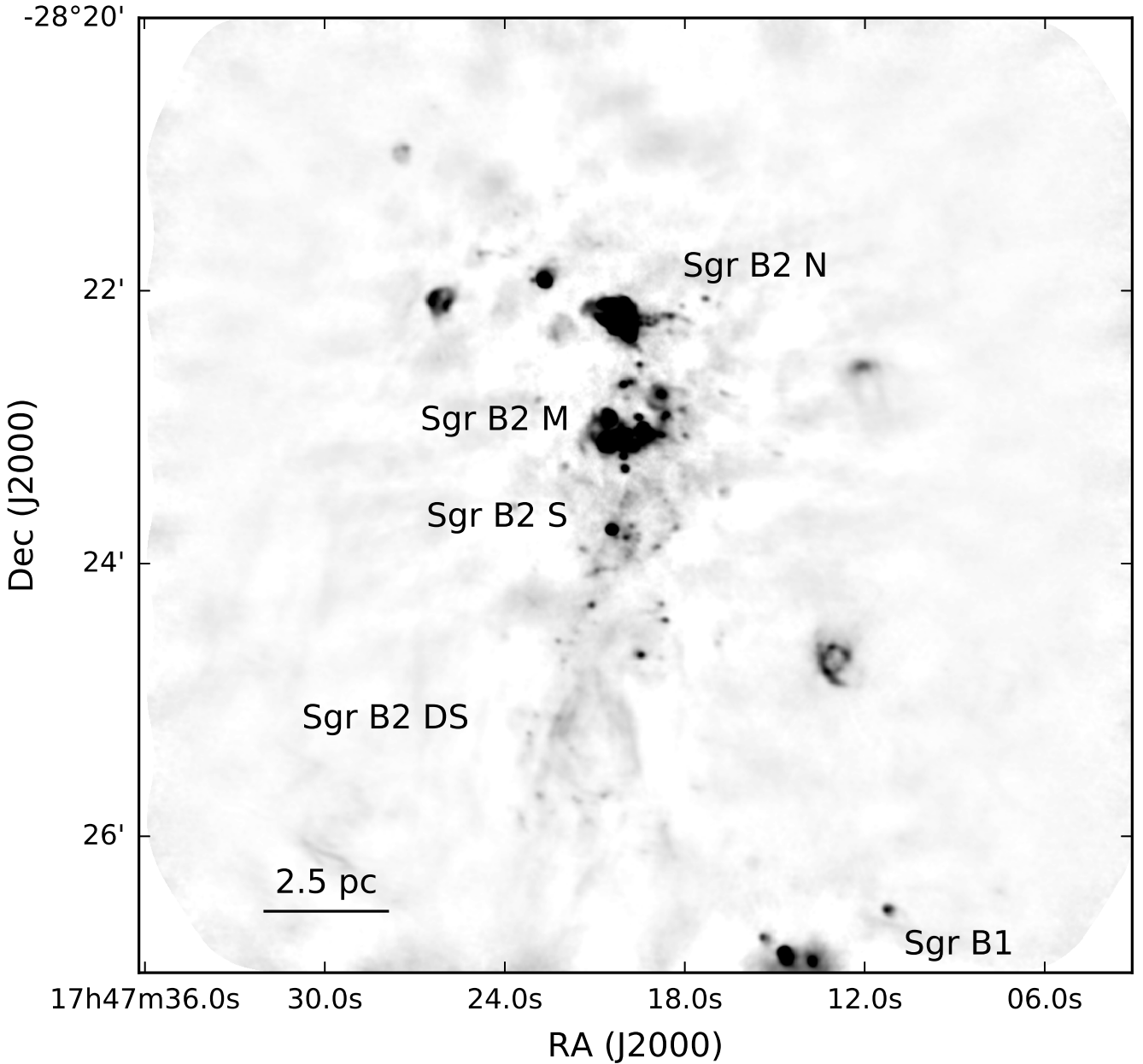


Figure 1. An overview of the Sgr B2 region, with the most prominent clusters labeled. The image shows the 3 mm observations here, imaged with $1.5''$ resolution to emphasize the larger scale emission features. For a cartoon version of this figure, see Schmiedeke et al. (2016) Figure 1

2.2. Other data - Column Density Maps

We use archival data from SCUBA, SHARC, and Herschel to create column density maps. We combined the SHARC and SCUBA data with Herschel SPIRE 350 and 500 μm images (Molinari et al. 2010), respectively. The data combination is discussed in detail in Appendix A.

The SHARC data were reported in Bally et al. (2010) and have a nominal resolution of $9''$ at 350 μm , however, at this resolution, the SHARC data display a much higher surface brightness than the Herschel data on the

same angular scale. An assumed resolution of $11.5''$ gives a better surface brightness match and is consistent with the measured scale of Sgr B2 N in the image. This calibration difference is likely to have been a combination of blurring by pointing errors, surface imperfections, and the gridding process, and flux calibration errors. In any case, the Herschel data provide the most trustworthy absolute calibration scale.

The SCUBA 450 μm data were reported in Pierce-Price et al. (2000) and Di Francesco et al. (2008) with

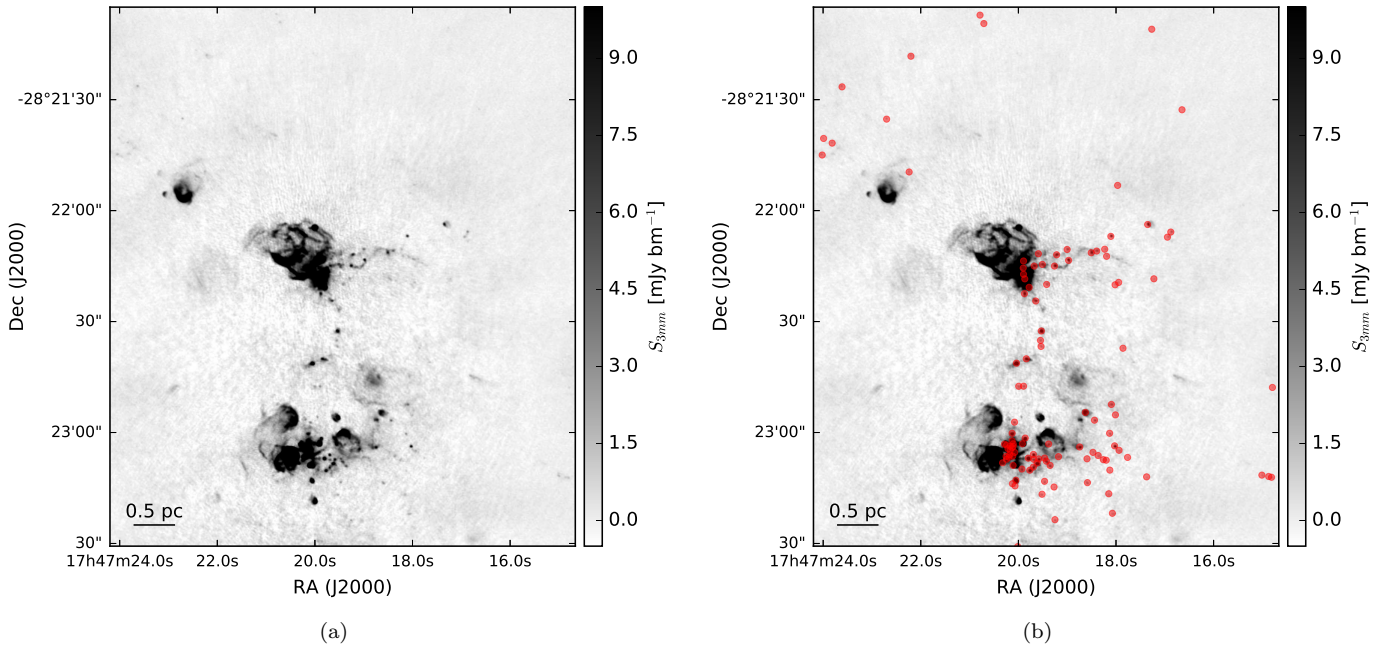


Figure 2. Images of the 3 mm continuum in the Sgr B2 M and N region. The right figure includes a red dot at the position of each identified continuum pointlike source. The massive protocluster Sgr B2 M is the collection of H II regions and compact source in the lower half of the image. The other massive protocluster, Sgr B2 N, is in the center. Imaging artifacts are evident at the 1-2 mJy bm^{-1} level.

Table 1. Observation Summary

Date	Array	Total Observing Time	Longest Baseline Length
		seconds	meters
01-Jul-2014	7.0	4045	49
02-Jul-2014	7.0	4043	49
03-Jul-2014	7.0	7345	48
06-Dec-2014	12.0	6849	349
01-Apr-2015	12.0	3464	328
02-Apr-2015	12.0	3517	328
01-Jul-2015	12.0	3517	1574
02-Jul-2015	12.0	10598	1574

a resolution of $8''$. We found that the SCUBA data had a flux scale significantly discrepant from the Herschel data, even accounting for the central wavelength difference. We had to scale the SCUBA data up by a factor ≈ 3.0 to make the data agree with the Herschel images on the angular scales they are both hypothetically sensitive to. While such a large flux calibration error seems implausible, the measured FWHM toward Sgr B2 N is approximately $14''$, which means the beam area is $\approx 3\times$ larger than the theoretical size. We attempted to fit several other isolated sources in the large SCUBA map, and the smallest FWHM we measured was

$\approx 10.5''$. Between the larger beam area, flux calibration errors (quoted at 20% in Pierce-Price et al. 2000), and the dust emissivity correction (35-50% for $\beta = 3 - 4$), this large flux scaling factor is actually plausible. This large correction factor is consistent with the large error beam found by Di Francesco et al. (2008), with effective FWHM $\approx 17.3''$, since they used additional smoothing when creating their maps.

To determine the column density, we use the Herschel data to perform SED fits to each pixel (Battersby et al, in prep). We performed these fits at $25''$ resolution,

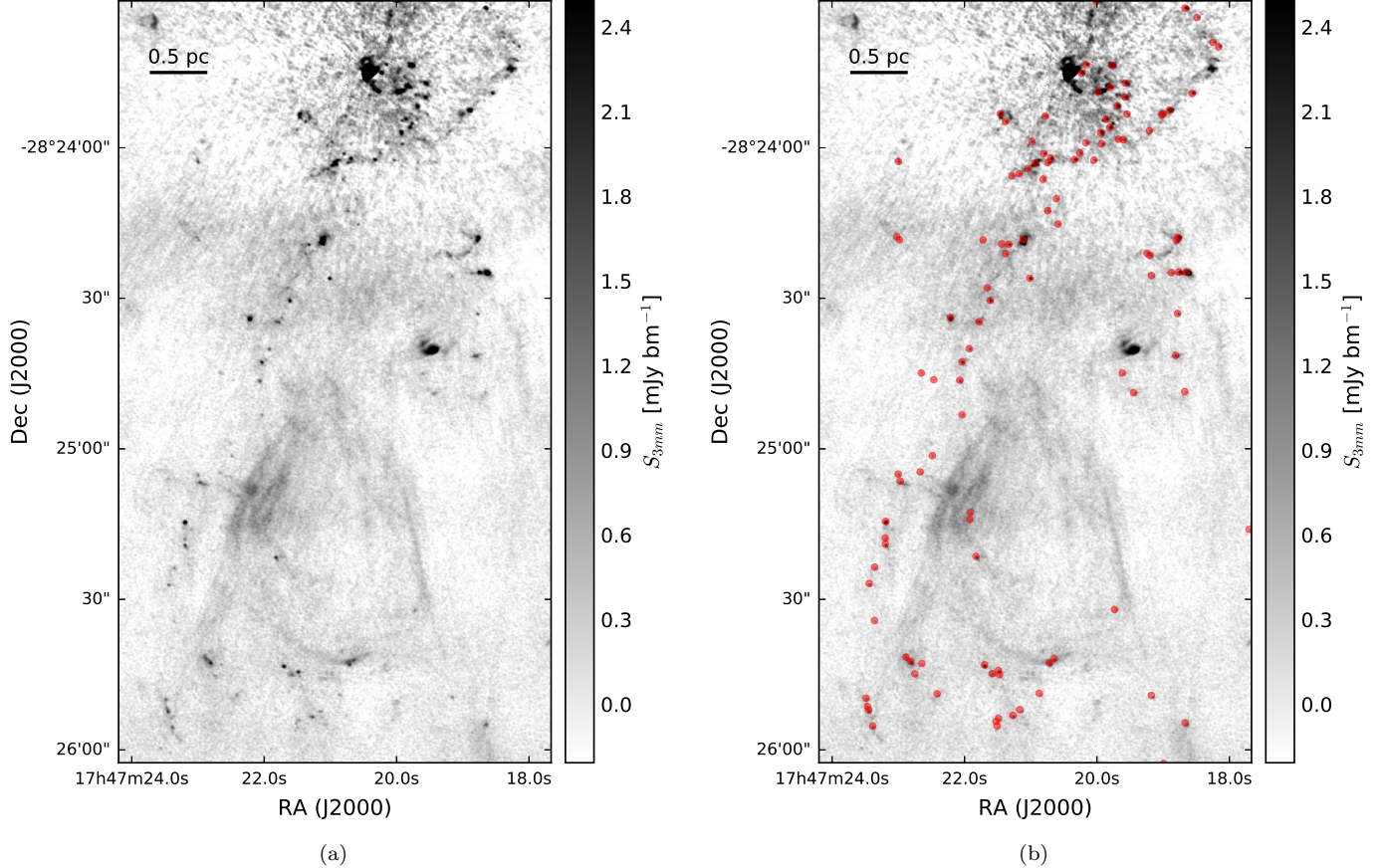


Figure 3. Images of the 3 mm continuum in the Sgr B2 DS region. The right figure includes a red dot at the position of each identified continuum pointlike source. The H II region Sgr B2 S is the bright source at the top of the image; imaging artifacts can be seen surrounding it. The largest angular scales are noisier than the small scales; the $\sim 20''$ -wide east-west ridge at around $-28:24:30$ is likely to be an imaging artifact. By contrast, the diffuse components in the southern half of the image are likely to be real.

using the 70, 160, 250, and 350 μm data and excluding the 500 μm channel.

To obtain higher resolution column density maps, we used the combined Herschel-SHARC and Herschel-SCUBA maps. We created several temperature maps, some assuming arbitrary constant temperatures equal to the minimum and maximum expected dust temperatures (20 and 50 K), and another using the temperature measured with Herschel interpolated onto the higher-resolution SCUBA and SHARC grids. Because of the interpolation or fixed temperature assumptions, the column maps are not very accurate and should not be used for systematic statistical analysis of the column density distribution without careful attention to the large implied uncertainties.

3. ANALYSIS

3.1. Continuum Source Identification

We selected continuum point sources as candidate cores or protostars by eye. An automated selection

is not viable across the majority of the field because there are many extended H II regions that dominate the overall map emission. A future automated selection algorithm may work if images at comparable resolution at other frequencies become available; the H II-region sources could then be excluded. Additionally, however, there are substantial imaging artifacts produced by the extremely bright emission sources in Sgr B2 M ($S_{3\text{mm},\text{max}} \approx 1.6$ Jy) and Sgr B2 N ($S_{3\text{mm},\text{max}} \approx 0.3$ Jy) that make automated source identification particularly challenging in the most source-dense regions. All of these features are evident in Figures 2 and 3.

Because the noise varies significantly across the map, a uniform selection criterion is not possible. We therefore include two levels of source identification, ‘high confidence’ sources, which are selected conservatively in regions of low-background, and ‘low-confidence’ sources that are somewhat lower signal-to-noise and are often in regions with higher background (labeled ‘conservative’ and ‘aggressive’ in Figure 4). Both of these selection

criteria are significantly more conservative than a local $5 - \sigma$ threshold.

We measure the local noise for each source by taking the median absolute deviation in an annulus 0.5 to 1.5'' around the source center. All but 7 sources have signal-to-local-noise ratios $S/N > 7$. These sources are all in regions of particularly high background or source density and therefore have overestimated local noise.

Our selection criteria result in a reliable but potentially incomplete catalog.

For a subset of the sources, primarily the brightest, we measured the spectral index α . We relied on CASA's α and $\sigma(\alpha)$ maps to obtain these measurements, including only those with $|\alpha| > 5\sigma(\alpha)$ or $\sigma(\alpha) < 0.1$. Several of the brightest sources did not have significant measurements of α because they are in the immediate neighborhood of Sgr B2 M or N and therefore have significantly higher background and noise, preventing a clear measurement.

We detected 243 compact continuum sources. Their flux distribution is shown in Figure 4. The distribution of their measured spectral indices α is shown in Figure 5.

3.2. Source Classification

For the majority of the detected sources, we have only a continuum detection at 3 mm. No lines are detected peaking toward most of the sources, especially the faint ones. A subset have detections at other bands and can be classified based on previous literature work, especially those associated with H II regions detected at 0.7 and 1.3 cm (Gaume et al. 1995; Mehringer et al. 1995; de Pree et al. 1996; Pree et al. 2015), which includes 78 sources. In this section, we employ various means to classify the sample of new sources.

We first note some key properties of dust at 3 mm. At 8.4 kpc, a 1 mJy source corresponds to an optically thin dust mass of $M(40K) = 18 M_{\odot}$ or $M(20K) = 38 M_{\odot}$ assuming a dust opacity index $\beta = 1.75$ ($\alpha = 3.75$ on the Rayleigh-Jeans tail) to extrapolate the Ossenkopf & Henning (1994) opacity to $\kappa_{3mm} = 0.0018 \text{ cm}^2 \text{ g}^{-1}$. Our dust-only 5- σ sensitivity limit at 40 K therefore ranges from $M > 7 M_{\odot}$ (0.5 mJy) to $M > 45 M_{\odot}$ (2.5 mJy) across the map. If we were to assume that these are all cold, dusty sources, as is typically (and reasonably) assumed for local clouds, they would be extremely massive and dense, with the lowest measurable density being $n(40K) > 3 \times 10^6 \text{ cm}^{-3}$ (corresponding to $7 M_{\odot}$ in a 0.5'' radius sphere). Such extreme objects are possible, but since we have detected > 100 of these sources, we evaluate other possibilities. We start with a few alternatives we are able to rule out.

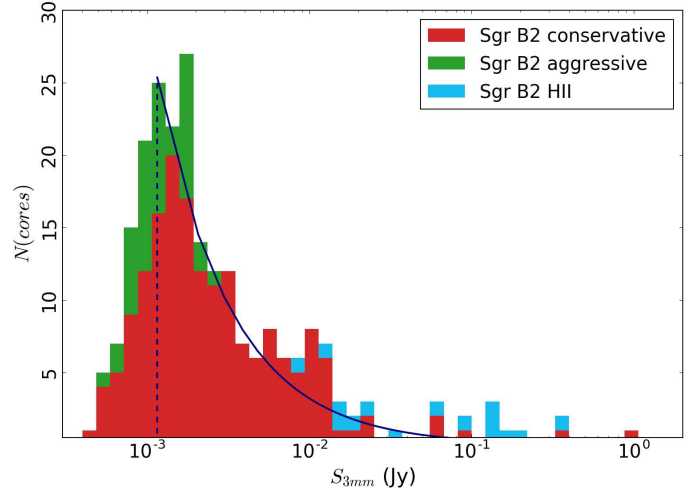


Figure 4. A histogram of the peak flux density of the observed sources with a powerlaw fit to the data excluding known H II regions. The powerlaw is an excellent fit, and it is shallower than the IMF slope, with $\alpha = 1.94 \pm 0.07$. The two brightest regions not identified as H II regions are Sgr B2M f1 and Sgr B2N K2; in these regions, it is unclear whether the free-free or dust emission dominates.

3.2.1. Alternative 1: The sources are externally ionized gas blobs

One possibility is that these sources are not dusty at all, nor pre- or protostellar, but are instead the brightest compact clumps surrounding diffuse H II regions. They would then be analogous to the heads of cometary clouds, externally ionized globules (“EGGs”), or proplyds, and their observed emission would give no clue to their nature because the light source is extrinsic.

The majority of the detected sources have size < 4000 AU, i.e., they are unresolved. By contrast, the free-floating EGGs ('frEGGs') so far observed have sizes 10,000-20,000 AU (Sahai et al. 2012a,b), so they would be resolved in our observations. Toward the brightest frEGG in Cygnus X, Sahai et al. (2012b) measured a peak intensity $S_{8.5GHz} \approx 1.5 \text{ mJy/beam}$ in a $\approx 3''$ beam. Cygnus X is 6× closer than the Galactic center, so their beam size is the same physical scale as ours. If the free-free emission is thin, the brightness in our data would be $S_{95GHz} = (95/8.5)^{-0.1} S_{8.5GHz} = 0.79 S_{8.5GHz} \approx 1.2 \text{ mJy/beam}$. These frEGGs would be detectable in our data. Comparison to radio observations at a comparable resolution will be needed to rule out the externally ionized globule hypothesis for the resolved regions within our sample, but the unresolved sources are unlikely to be frEGGs.

If the detected sources were either EGGs or cometary clouds, we would expect them to be located within diffuse H II regions. Many of the sources are near H II re-

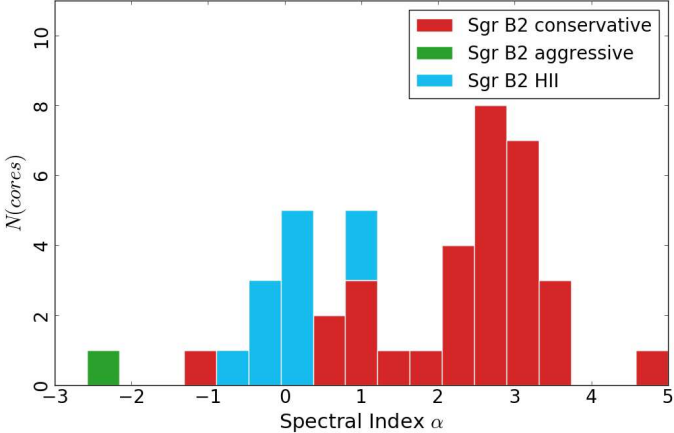


Figure 5. A histogram of the spectral index α for those sources with a statistically significant measurement. The H II regions cluster around $\alpha = 0$, as expected for optically thin free-free emission, while the unclassified sources cluster around $\alpha = 3$, which is weakly consistent with dust emission. There are two particularly notable outliers: the source with a highly negative spectral index, Source 167, has a statistically significant measurement but is in a region of particularly high extended and diffuse background, so the measurement may not be reliable. The other unidentified source with $\alpha \sim -1$ is Source 80, which is very close to the H II region Sgr B2 S, but is not detected in the de Pree et al. (1996) 1.3 cm data; it may be an H II region or it may be contaminated by the nearby H II region.

gions, as seen in Figure 6a. However, they are nearly all associated with a ridge of HC₃N emission (Figure 6b). If they are deeply embedded within the molecular material, they cannot be externally ionized. The fact that the ionized gas is brightest nearby, rather than directly on top of, the HC₃N suggests that the HC₃N traces a full molecular cloud rather than a thin PDR-like layer.

A final point against the externally ionized hypothesis is the observed spectral indices shown in Figure 5. We measured spectral indices for 43 sources, of which 23 have $\alpha > 2$. These sources are inconsistent with free-free emission and are at least reasonably consistent with dust emission.

3.2.2. Alternative 2: The sources are H II regions produced by interloper ionizing stars

If there is a large population of older (age 1-30 Myr) massive stars, they could ignite compact H II regions when they fly through molecular material. See 3.2.3 for calculations of stationary H II region properties. The main problem with this scenario is the spatial distribution of the observed sources. While most of the continuum sources are associated with dense gas and dust ridges, not all of the high-column molecular gas regions have such sources in them (i.e., the left and right sides

of the image in Figure 6b, where molecular material is seen with no associated millimeter sources). If there is a free-floating population of OB stars responsible for the 3 mm point source population, if we assume the spatial distribution of the stars is uniform, the distribution of H II regions surrounding them should match of the gas (since we are assuming the gas and stars are moving independently). Also, there is no such population of sources seen outside of the dense gas in the infrared (TODO: Who has done infrared studies of Sgr B2? You can infer what I have stated ‘by inspection’ of 2MASS, but it would be more straightforward to quote someone else), which again we should expect if there is a uniformly distributed population. Finally, the spectral indices discussed above (Figure 5) suggest the previously-unidentified sources are dust emission sources, not free-free sources.

3.2.3. Alternative 3: The sources are H II regions produced by recently-formed OB stars

For an unresolved spherically symmetric H II region ($R = 4000$ AU), the expected flux density is $S_{95\text{GHz}} = 4.7$ mJy for a $Q_{lyc} = 10^{47}$ s⁻¹ source (assuming $T_e = 7000$ K), and that value scales linearly with Q_{lyc} as long as the source is optically thin. Rearranging Condon & Ransom (2007) equations 4.60 and 4.61:

$$\begin{aligned} S_\nu(Q_{lyc}) &= 4.67 [1 - \exp(c_* T_* \nu_* EM_*)] \\ \nu_* &= \left(\frac{\nu}{\text{GHz}}\right)^{-2.1} \\ T_* &= \left(\frac{T_e}{10^4 \text{K}}\right)^{-1.35} \\ c_* &= -3.28 \times 10^{-7} \\ EM_* &= \frac{3Q_{lyc}}{4\pi R^2 \alpha_b} \end{aligned} \quad (1)$$

where $\alpha_b = 2 \times 10^{-13}$ cm³ s⁻¹, Q_{lyc} is the count rate of ionizing photons in s⁻¹, and R is the H II region radius.

An extremely compact H II region, e.g., one with $R < 100$ AU and corresponding density $n > 10^6$ cm⁻³, would be optically thick and therefore fainter, $S_{95\text{GHz}}(R = 100\text{AU}, Q_{lyc} = 10^{47}\text{s}^{-1}) = 3.4$ mJy. Even the brightest O-stars could produce H II regions as faint as 0.5 mJy if embedded in extremely high density gas; above $Q_{lyc} > 10^{47}$ s⁻¹, a 25 AU H II region would be ~ 0.5 mJy.

Figure 7 shows the predicted brightness for various H II regions produced by OB stars and the density required for those H II regions to be the specified size. In order for the detected sources to be O-star-driven H II regions, with $10^{47} < Q_{lyc} < 10^{50}$ s⁻¹, they must be optically thick and therefore extremely compact and

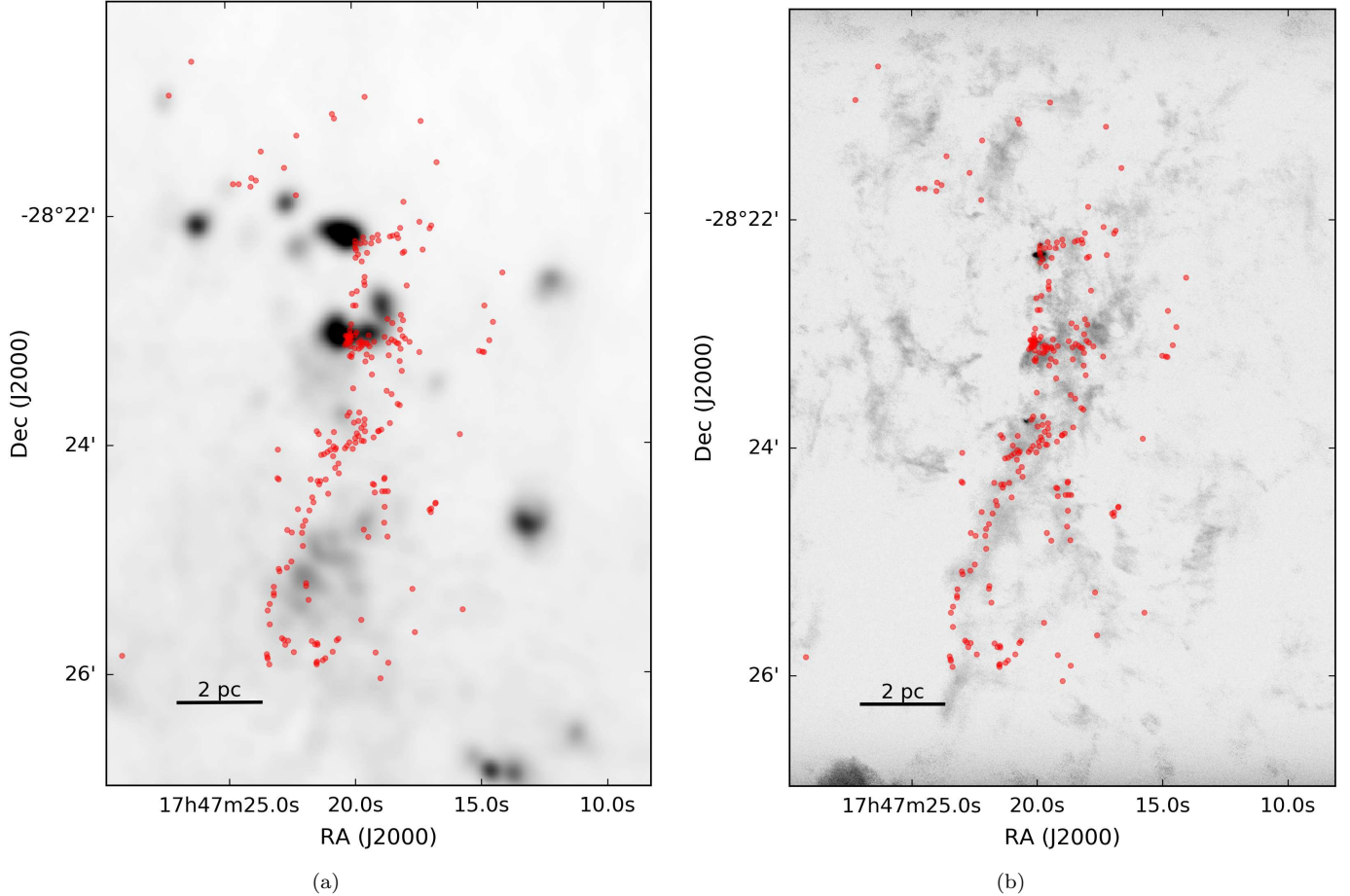


Figure 6. (left) The location of the detected continuum sources (red points) overlaid on a 20 cm continuum VLA map highlighting the diffuse free-free (or possibly synchrotron) emission in the region (Yusef-Zadeh et al. 2004). (right) Continuum sources overlaid on a map of the HC₃N peak intensity. HC₃N traces moderate-density molecular gas.

dense. There is a narrow range of late O/early B stars, $10^{46} < Q_{lyc} < 10^{47}$ s $^{-1}$, that could be embedded in compact H II regions of almost any size and produce the observed range of flux densities. Anything fainter, later than \sim B0 ($Q_{lyc} < 10^{46}$ s $^{-1}$), would be incapable of producing the observed flux densities. Any brighter stars would have to be embedded in dust that, at 40 K, would outshine the H II region; more likely, such sources would have much hotter dust and therefore would be much brighter (and more extended) than our observations allow.

This restrictive parameter space, combined with a steep luminosity function that implies there are many more sources at slightly lower luminosity, is evidence against the population being dominated by H II regions. The spectral indices also support this conclusion, since many are steeper than $\alpha > 2$ and are therefore inconsistent with free-free emission.

3.2.4. The sources are protostars

After ruling out the other hypotheses, we conclude that these sources are predominantly embedded protostars. Their emission is likely dust-dominated, but is probably warmer than the cloud average $\sim 20 - 40$ K. We test and validate the hypothesis that most or all of the sources are protostellar in this section.

We cross-matched our source catalog with catalogs of H II regions and methanol masers. Class II methanol masers are always associated with sites of high-mass star formation. The Caswell et al. (2010) Methanol Multi-beam Survey identified 11 sources in our observed field of view, of which 10 have a clear match in our catalog. Several other sources in our catalog match known H II regions from Gaume et al. (1995), mostly associated with the brightest sources in our sample; these all have $S_{3\text{mm}} > 9$ mJy. Additionally, some of the sources have X-ray counterparts in the Muno et al. (2009) Chandra point source catalog.

We compare our detected sample to that of the Herschel Orion Protostar Survey (HOPS; Furlan et al. 2016)

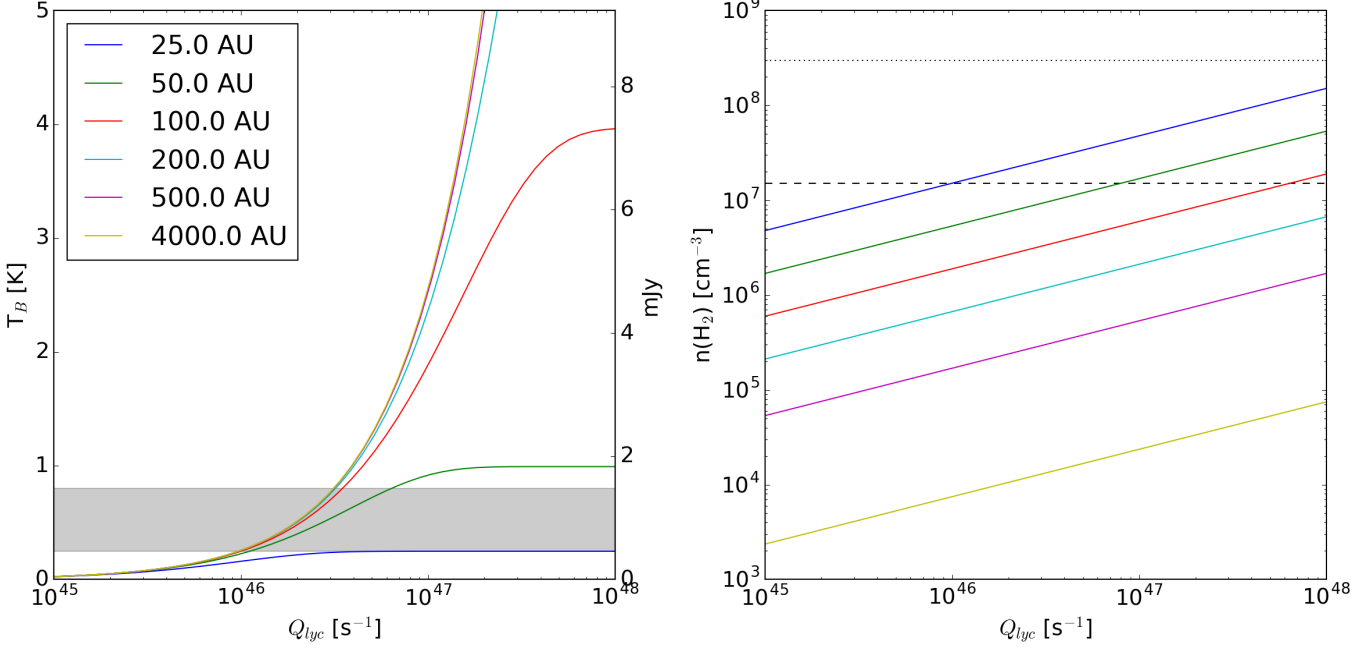


Figure 7. Simple models of spherical H II regions to illustrate the observable properties of such regions. The H II region size is shown by line color; the legend in the left plot applies to both figures. (left) The expected brightness temperature (left axis) and corresponding flux density within a FWHM=0.5'' beam (right axis) as a function of the Lyman continuum luminosity for a variety of source radii. The grey filled region shows the range of our 5-sigma sensitivity limits, which vary with location from 0.25 to 0.8 K. (right) The density required to produce an H II region of that radius. The horizontal dashed line shows the density corresponding to an unresolved dust source at the 5- σ detection limit (≈ 0.5 mJy, or about $10 M_{\odot}$ of dust, assuming $T = 40$ K). Above this line, dust emission would dominate over free-free emission. The dotted line shows the density required for dust emission to produce a 10 mJy source at $T = 40$ K. As seen in the left plot, for any moderate-sized H II region, $R > 100$ AU, a high-luminosity star ($Q_{lyc} > 10^{47} \text{ s}^{-1}$) would produce an H II region brighter than the majority of our sample, which includes only a few sources brighter than 10 mJy. The electron densities required to produce H II regions within our observed range ($1 < S_{\nu} < 10 \text{ mJy}$) are fairly extreme, $n_e \gtrsim 10^6 \text{ cm}^{-3}$, for O-stars.

in order to get a general sense of what types of sources we have detected. We selected this survey for comparison because it is one of the largest protostellar core samples with well-characterized bolometric luminosities available. Figure 8 shows the HOPS source fluxes at $870 \mu\text{m}$ scaled to 3 mm assuming a dust opacity index $\beta = 1.5$, which is shallower than usually inferred, so the extrapolated fluxes may be slightly overestimated. The $870 \mu\text{m}$ data were acquired with a $\sim 20''$ FWHM beam, which translates to a resolution $\sim 1''$ at $d_{SgrB2} = 8.4 \text{ kpc}$ assuming $d_{Orion} = 415 \text{ pc}$, so our beam size is somewhat smaller than theirs. The HOPS sources are all fainter than the Sgr B2 sources. The brightest HOPS source, with $L_{tot} < 2000 L_{\odot}$, would only be 0.2 mJy in Sgr B2, or about a 4- σ source - below our detection threshold even in the noise-free regions of the map. We conclude that the Sgr B2 sources are much more luminous and are therefore massive protostars.

This conclusion is supported by a more direct comparison with the Orion nebula as observed at 3 mm with MUSTANG (Dicker et al. 2009, Figure 9). Their data were taken at $9''$ FWHM resolution, correspond-

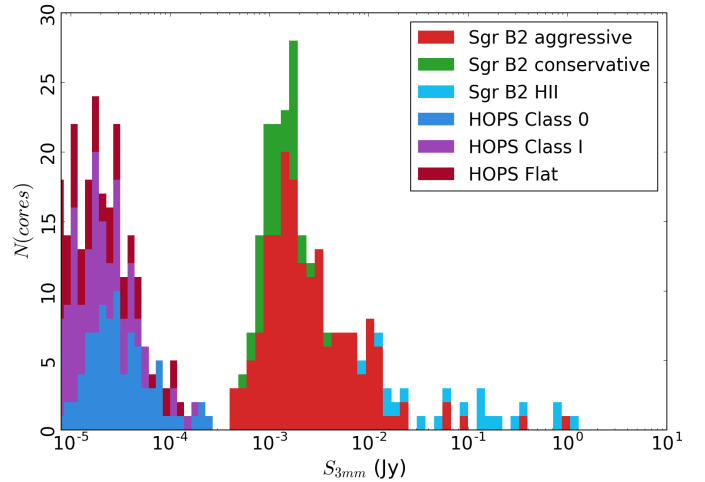


Figure 8. A histogram combining the detected Sgr B2 cores with predicted flux densities based on the HOPS (Furlan et al. 2016) survey. The HOPS histogram shows the $870 \mu\text{m}$ data from that survey scaled to 3 mm assuming $\beta = 1.5$. Every HOPS source is well below the detection threshold for our observations.

ing to $0.48''$ at d_{SgrB2} . The peak flux density measured in that map is toward Source I, $S_{90GHz}(d_{SgrB2}) = 3.6$ mJy. Source I would therefore be detected and would be somewhere in the middle of our sample. It is extended, and the extended component would be readily detected in our data. Since Source I is the only known high-mass YSO in the Orion cloud, and it would be detectable while no other sources in the Orion cloud would be, it appears safe to conclude that all of our detected sources are MYSOs.

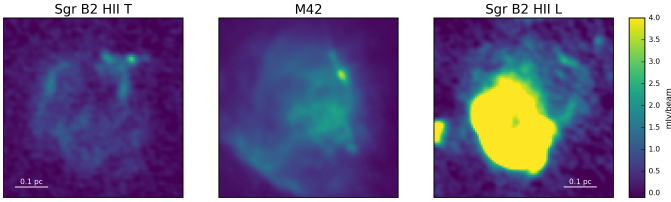


Figure 9. Comparison of two extended H II regions in Sgr B2 to the M42 nebula in Orion. The three panels are shown on the same physical and color scale assuming $d_{Orion} = 415$ pc and $d_{SgrB2} = 8.4$ kpc and that the ALMA and MUSTANG data have the same continuum bandpass. Sgr B2 H II T is comparable in brightness and extent to M42; Sgr B2 H II L is much brighter and is saturated on the displayed brightness scale. The compact source to the top right of the M42 image is Orion Source I; the images demonstrate that Source I and the entire M42 nebula would be easily detected in our data.

While we have concluded that the sources are dusty, massive protostars, the spectral indices we measured are somewhat surprising. Typical dust clouds in the Galactic disk have dust opacity indices $\beta \sim 1.5 - 2$ (Schnee et al. 2010; Shirley et al. 2011; Sadavoy et al. 2016). Our spectral indices are lower than these, with only 3 sources having measured $\beta = \alpha - 2 > 1.5$ (at the 2σ level, up to 11 sources are consistent with $\beta = 1.5$, but this is primarily because of their high measurement error). A shallower β implies free-free contamination, large dust grains, or optically thick surfaces are present within our sources. Since the above arguments suggest that the sources are high-mass protostars, the free-free contamination and optically thick inner region models are both plausible.

3.3. Source distribution functions and the star formation rate

In this section we examine the flux density distribution of the observed sources and the implied total stellar masses.

The flux density distribution of the non-H II region sources follows a powerlaw with slope $\alpha = 1.94 \pm 0.07$ (fitted with the MLE method of Clauset et al. 2007). If we assume (incorrectly) that the stellar mass is lin-

early proportional to the 3 mm continuum flux density, this measurement implies a slope shallower than the $\alpha \sim 2.35$ expected for a normal IMF. It is possible that the IMF is genuinely different from Salpeter here, but it is more likely that the more massive stars are surrounded by warmer gas, implying that the source mass distribution is steeper than the source flux distribution.

If we make the very simplistic assumptions that the sources we detect are all $L \gtrsim 2000 L_\odot$ ($M \gtrsim 8M_\odot$), we can infer the total (proto)stellar mass in the observed region. Using a Kroupa (2001) mass function with $M_{max} = 200 M_\odot$, 23% of the mass is contained in $M > 8M_\odot$ stars. Using $M = 8M_\odot$ as the lower-limit case for each source, the identified sources have total mass $M(> 8) = 1800 M_\odot$. The total stellar mass implied is $M_{tot} = 8 \times 10^3 M_\odot$. If instead we assume each source has a mass equal to the mean stellar mass for $M > 8 M_\odot$, $\bar{M} = 21.1 M_\odot$, then the total inferred stellar mass is $M_{tot} = 2 \times 10^4 M_\odot$. These are lower limits in the Sgr B2 N and M regions because our catalog is incomplete due to confusion and dynamic range limitations. Additionally, we are using a single-star IMF and our resolution is only ~ 4000 AU, so it is likely that we have undercounted by $\gtrsim 2\times$, since high-mass stars have a high multiplicity fraction (Mason et al. 2009).

For each subcluster identified in Schmiedeke et al. (2016), we count the number of H II regions identified in our survey plus those identified in previous works (de Pree et al. 1996), and we count the number of protostellar cores not associated with H II regions. To estimate the stellar mass, we assume each core contains a star with $M(8 - 20) = 12 M_\odot$ and each H II region contains a $\geq B0$ star with $M(> 20) = 45 M_\odot$. In Table 2, this estimate is shown as M_{obs} . We also compute the total stellar mass using the mass fractions $f(M > 20) = 0.14$ and $f(8 < M < 20) = 0.09$. The inferred masses computed from H II region counts and from core counts are shown in columns $M_{inferred,HII}$ and $M_{inferred,cores}$ respectively; $M_{inferred}$ is the average of these two estimates. If our assumptions are correct and the mass distribution is governed by a power-law IMF, we expect $M_{inferred,HII} = M_{inferred,cores}$. Except for Sgr B2 M, the core-based and H II-region based estimates agree to within $\sim 25\%$, which is about as good as expected from Poisson noise in the counting statistics.

Sgr B2 M has the largest sample in both counts and has a factor of nine discrepancy. The discrepancy may arise from the combined effects of source confusion at our $0.5''$ resolution and the increased noise around the extremely bright central region that makes detection of < 2 mJy sources difficult. The majority of pixels within the cluster region have significant detections at 3 mm,

but we do not presently have the capability to distinguish between extended dust emission, free-free emission, or a confusion-limited point source population.

We compare our mass estimates to those of Schmiedeke et al. (2016), who inferred stellar masses primarily from H II region counts. The last two columns of Table 2 show the observed and estimated masses based on H II region counts. For Sgr B2 M and N, our results are similar, as expected since our catalogs are similar. For S and NE, we differ by a large factor, primarily because Schmiedeke et al. (2016) assumed that $M_{min,MYSO}$ and M_{max} were the smallest and largest observed masses in the cluster, while we assumed $M_{min,MYSO} = 8 M_\odot$ and $M_{max} = 200 M_\odot$; i.e., we assumed a spatially invariant IMF.

To determine the star formation rate, we need to know the age of the current star forming burst. We can use the dynamical model of Kruijssen et al. (2015) to get an age of the Sgr B2 cloud $t = 0.74$ Myr. To infer the star formation rate, we divide the observed mass by this age; the results are shown in 2. This rate assumes that star formation was initiated by the cloud’s most recent pericenter passage. The total inferred SFR of the Sgr B2 cloud is $0.036 M_\odot \text{ Myr}^{-1}$, between one quarter and one half of the total for the CMZ (Longmore et al. 2013; Barnes et al. 2017).

3.4. An examination of star formation thresholds

Many authors (e.g., Lada et al. 2010) have proposed that star formation can only occur above a certain density or column density threshold¹. We discuss our measurements of column thresholds in this Section.

3.4.1. Comparison to Lada, Lombardi, and Alves 2010

In this section, we compare the star formation threshold in Sgr B2 to that in local clouds performed by Lada et al. (2010). They determined that all star formation in local clouds occurs above a column density threshold $M_{thresh} > 116 M_\odot \text{ pc}^{-2}$, or $N_{thresh}(\text{H}_2) > 5.2 \times 10^{21} \text{ cm}^{-2}$ assuming the mean particle mass is 2.8 amu (Kauffmann et al. 2008). We first note, then, that *all pixels* in our column density maps are above this threshold by *at least* a factor of 10.

However, Sgr B2 is 8.4 kpc away from us in the direction of our Galaxy’s center, meaning there is a potentially enormous amount of material unassociated with the Sgr B2 cloud along the line of sight. This material

¹Column density is more commonly used because of its observational convenience, but it is physically meaningless unless high column density leads to high optical depths and thereby changes the gas’s ability to cool.

may have column densities as low as $5 \times 10^{21} \text{ cm}^{-2}$ or as high as $5 \times 10^{22} \text{ cm}^{-2}$, as measured from relatively blank regions in the Herschel column density map (Battersby et al. 2011). The former value corresponds to the background at high latitudes, $b \sim 0.5$, while the latter is approximately the lowest seen within our field of view. Even with the very aggressive foreground value of $5 \times 10^{22} \text{ cm}^{-2}$ subtracted, nearly the whole Sgr B2 cloud exists above this threshold.

To directly compare our observations to the star formation thresholds reported in Lada et al. (2010), we examined the column density associated with each millimeter continuum source. The Lada et al. (2010) data used a variable resolution for the column measurements toward their sample, ranging from 0.06–0.35 pc (equivalent to 1.5 to $9.2''$ at a distance of 8.4 kpc). The Herschel data we have available with per-pixel SED fits lack the resolution needed to make a direct comparison to the Lada et al. data set, but the SHARC and SCUBA data have resolution approximately equivalent to that used in the Orion molecular cloud in their survey. We therefore use a range of temperatures bracketing the observed range in the Herschel maps ($\sim 20 - 50$ K) to produce column density maps from the SCUBA and SHARC data. Figure 10 shows the cumulative distribution function of the column density associated with each identified continuum source; the column density used is the nearest-neighbor pixel to the source in the column density maps. Even using the conservative maximum temperature $T_{dust} = 50$ K (resulting in the minimum column density), all of the sources exist at a column density an order of magnitude higher than the Lada threshold, and they exist above that threshold even if the foreground is assumed to be an extreme $5 \times 10^{22} \text{ cm}^{-2}$.

The Lada et al. (2010) sample used Spitzer observations of nearby clouds that were nearly complete to stars at least as small as $0.5 M_\odot$. By contrast, as discussed in Section 3.2.4, our survey is sensitive only to stars with $M \gtrsim 8 M_\odot$. The apparently higher threshold either means that there is a genuinely higher threshold for star formation in the CMZ or that there is a higher threshold for high-mass star formation that may still be universal.

3.4.2. Comparison to other CMZ clouds

In G0.253+0.016 (The Brick, G0.253), very little star formation has been observed (Longmore et al. 2013; Johnston et al. 2014; Rathborne et al. 2015) despite most of the cloud existing above the locally measured Lada et al. (2010) column density threshold. The col-

Table 2. Cluster Masses

Name	$N(\text{cores})$	$N(\text{HII})$	M_{count}	M_{inferred}	$M_{\text{inferred,HII}}$	$M_{\text{inferred,cores}}$	M_{count}^s	M_{inf}^s	SFR
			M_{\odot}	M_{\odot}	M_{\odot}	M_{\odot}	M_{\odot}	M_{\odot}	$M_{\odot} \text{ kyr}^{-1}$
M	18	51	2500	9500	17000	2400	1295	20700	13
N	10	7	440	1800	2300	1400	150	2400	2.5
NE	4	2	140	600	650	540	52	1200	0.81
S	3	1	81	370	330	410	50	1100	0.5
Total	221	72	5900	27000	24000	30000	1993	33400	36

M_{count} is the mass of directly counted protostars, assuming each millimeter source is $12.0 M_{\odot}$, or $45.5 M_{\odot}$ if it is also an H II region. $M_{\text{inferred,cores}}$ and $M_{\text{inferred,HII}}$ are the inferred total stellar masses assuming the counted objects represent fractions of the total mass 0.09 (cores) and 0.14 (H II regions). M_{inferred} is the average of these two. M_{count}^s and M_{inf}^s are the counted and inferred masses reported in Schmiedeke et al. (2016). The star formation rate is computed using an age $t = 0.74$ Myr, which is the time of the last pericenter passage in the Kruijssen et al. (2015) model.

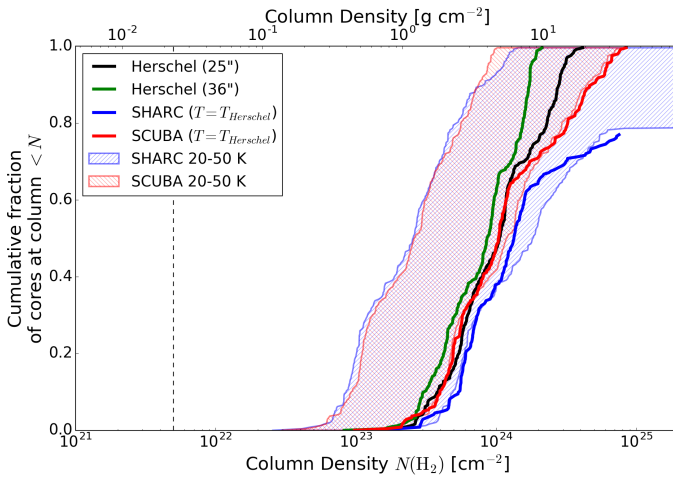


Figure 10. Cumulative distribution functions of the background column density associated with each identified 3 mm continuum source. The column densities are computed from a variety of maps with different resolution and assumed temperature. The Herschel maps use SED-fitted temperatures (Battersby et al. 2017) at $25''$ resolution (excluding the $500 \mu\text{m}$ data point) and $36''$ resolution. The SHARC $350 \mu\text{m}$ and SCUBA $450 \mu\text{m}$ maps both have higher resolution ($\sim 10''$) but no temperature information; we used an assumed $T_{dust} = 20$ and $T_{dust} = 50$ K to illustrate the range of possible background column densities (hatched red and blue). The thick solid red and blue lines show the SHARC and SCUBA column density images using Herschel temperatures interpolated onto their grids: these curves are closer to the 20 K than the 50 K curve and serve as the best estimate column density maps. The SHARC data fail to go to a cumulative fraction of 1 because the central pixels around Sgr B2 M and N are saturated (the lower temperature assumptions result in optical depths > 1 , which cannot be converted to column densities using the optically thin assumption). The vertical dashed line shows the $N(\text{H}_2) = 5.2 \times 10^{21} \text{ cm}^{-2}$ column density threshold from Lada et al. (2010).

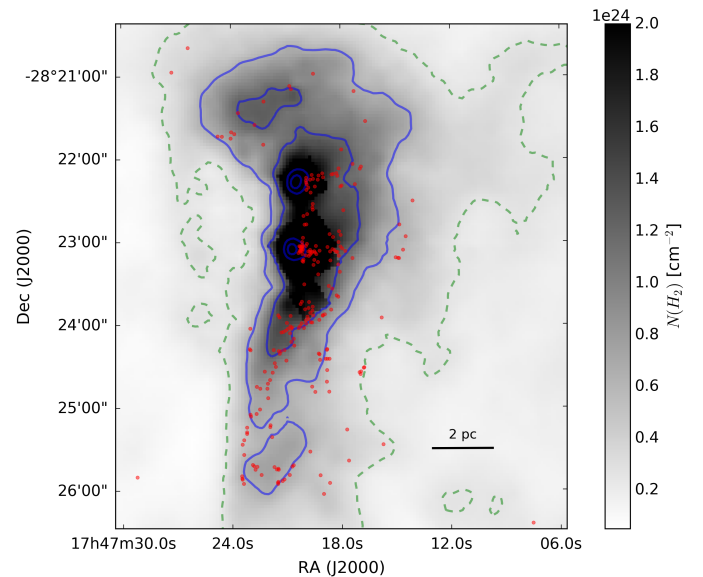


Figure 11. Overlay of the core and HCH II region locations on the SCUBA column density map created by interpolating the Herschel-measured temperatures onto the SCUBA grid and assuming the dust is optically thin at $450 \mu\text{m}$. The square grid at the center shows a region affected by saturation in the Herschel data. Contours are shown at $N(\text{H}_2) = 2 \times 10^{23} \text{ cm}^{-2}$ (green dashed lines) and $N(\text{H}_2) = 5, 10, 50, 100 \times 10^{23} \text{ cm}^{-2}$ (blue lines). As shown in Figure 10, the threshold above which nearly all cores are found is high, but this figure shows that the core density is not well-correlated with the column density: there is a relative dearth of cores in the high-column north region and an overabundance in the moderate-column deep south region.

umn density distribution function for G0.253 is shown in Figure 12.

Comparing Sgr B2 to G0.253, the majority of the Sgr B2 cloud is at higher column than G0.253. The presence of star formation in Sgr B2 nearly all occurs at a higher column than exists within G0.253 (Figure 12). The lack

of observed cores in The Brick is therefore consistent with the active SF seen in Sgr B2.

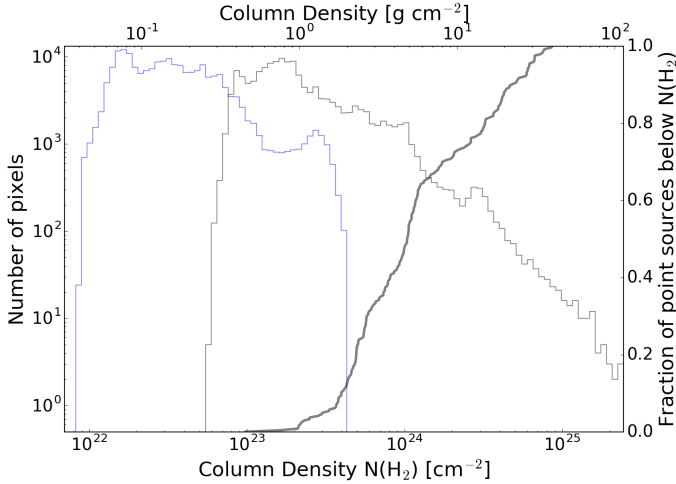


Figure 12. Histograms of the column density of G0.253+0.016 (blue) and Sgr B2 (gray) using the combined SCUBA 450 μm and Herschel 500 μm intensity with the interpolated Herschel dust temperatures. The cumulative distribution of core ‘background’ column densities in Sgr B2 is shown as a thick gray line.

4. DISCUSSION

We have reported the detection of a large number of point sources and inferred that they are most likely all high-mass protostars. These sources universally reside in gas above $N \gtrsim 2 \times 10^{23} \text{ cm}^{-2}$. In this section, we discuss the implications of this apparent threshold for high-mass star formation in the CMZ.

A theoretical threshold for high-mass star formation, $N > 1 \text{ g cm}^{-2}$ was developed by Krumholz & McKee (2008). Nearly all of the sources we have detected reside above this threshold, and we determined our sources are all likely to be massive protostars in Section 3.2.4. However, not all pixels with $N > 1 \text{ g cm}^{-2}$ are forming high-mass stars (Figure 13). We have therefore apparently confirmed that this threshold is a necessary, but not sufficient, condition for high-mass star formation.

4.1. What drives star formation in the greater Sgr B2 complex?

We have shown that, in addition to the known forming massive clusters, star formation is ongoing in an extended and elongated region to the north and south. Excluding the clusters, most of the newly discovered sources trace out long and linear features. Why are the sources aligned? Was star formation in Sgr B2 triggered by a single event?

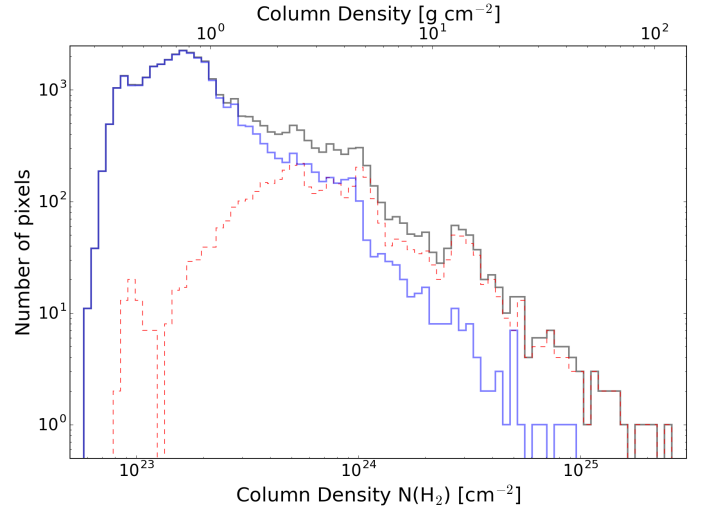


Figure 13. Histograms of the column density measured with the combined SCUBA and Herschel data using the interpolated Herschel temperatures covering only the region observed with ALMA. The black histogram shows the whole observed region, the blue solid shows the SCUBA pixels that do not contain an ALMA source, and the red dashed region shows those pixels that are within one beam FWHM of an ALMA source. While the ALMA sources (high mass protostars and young stars) clearly reside in high-column gas, there is abundant high-column material that shows no signs of ongoing star formation.

There are a few different possible triggers that have been considered in the literature: pericenter passage (Krijssen et al. 2015), cloud-cloud collision (Hasegawa et al. 1994; Mehringer & Menten 1997; Sato et al. 2000), and expanding shells driven by massive stars (Martín-Pintado et al. 1999). These scenarios are distinct and apply to different scales. The pericenter passage model assumes that gas is fed into a ~ 100 pc radius non-circular orbit and experiences significant compression at closest approach to the central cluster. The compression leads to progressively increasing star formation along the CMZ dust ridge. Cloud-cloud collision models assume that independent clouds on different orbits are interacting. The expanding shell model assumes the shells are driven by feedback from a previously formed generation of high-mass stars.

We examine these three possibilities but reach no definitive conclusion about which process is dominant.

4.1.1. Pericenter Triggering

Our observations are reconcilable with a star formation event triggered at pericenter passage. See Section 4.2.

4.1.2. Cloud-cloud collision

There are no definitive signs of ‘cloud-cloud collision’ or ‘colliding flows’ in our data. Most of the notable kinematic features evident in the dense gas images can be attributed to expanding H II regions or otherwise feedback-driven flows (see Section 4.1.3). While interacting independent gas streams are a possible agent affecting Sgr B2, their effects are not obvious in our core catalog or in the gas data cubes.

We note that some ‘colliding flows’ are expected in almost any collapse scenario. For example, simulations of a cloud passing through Galactic pericenter (Dale et al, in prep) show that some material is ejected during this passage that later collapses back onto the original cloud. It is possible that any apparent colliding flows are a relic of this process.

4.1.3. Expanding Shells

There is evidence of expanding shells in Sgr B2, but these shells are not uniformly sites of star formation. There are four shell examples we consider: Sgr B2 DS, Sgr B2 N/NE, Sgr B2 E, and Sgr B2 W. Two of these (N/NE and DS) show signs of star formation, two (E and W) do not.

There is extended ionized emission in Sgr B2 Deep South that appears to be a bubble surrounded by the millimeter continuum sources. While this region looks like a normal H II region in the 12'' resolution 20 cm VLA data in Figure 6, the 3 mm continuum reveals long filamentary features reminiscent of the Galactic center arched filaments. By analogy, they may be magnetically dominated regions, but there must be some central source of ionizing radiation or energetic particles. Whatever the driver, it is possible that an expanding bubble of hot gas has compressed the molecular material along the ridge where we observe star formation.

By contrast, the Sgr B2 North bubble does not contain any ionized emission. It contains fewer total sources, which trace the edge of an expanding bubble previously noted by de Vicente et al. (1997). The coincidence of star forming cores along the edge of a bubble again suggests some sort of compressional triggering.

However, while both N/NE and DS show circumstantial, morphological evidence for a compressional event, there are other regions within our map that show the same general morphology in the gas yet exhibit no star formation. Sgr B2 E and W are the regions east and west of the central ridge, respectively.

Shell-like features in Sgr B2 E can be seen in Figure 14. The molecular gas, as traced by HC₃N in this case, outlines bubble edges to the east of Sgr B2 M: the HC₃N outlines a cavity in the column density map. The edge of this eastern bubble has a lower average column density

than either the northern Sgr B2 NE or the Sgr B2 DS regions, and it shows no signs of ongoing star formation.

In Sgr B2 W, there is a secondary ridge of HC₃N emission paralleling the central ridge. No MYSOs are detected in this ridge.

While the expanding shells may have some effect on where MYSOs are forming, they do not provide a sufficient condition to drive star forming bursts.

4.2. The clusters and the extended population

We noted in Section 3.3 that the H II-region-inferred protostellar mass matches the core-inferred protostellar mass to within a factor of 2 in the whole Sgr B2 cloud and the individual clusters excepting Sgr B2 M. In Sgr B2 M, the H II-region inferred mass is $\sim 9 \times$ greater than the core-inferred mass. While the lack of faint sources in Sgr B2 M could be an observational limitation, it may also be physical.

Sgr B2 M has more H II regions and is more centrally condensed than any of the other clusters and the distributed star forming population. Assuming that H II regions represent a later stage in protostellar evolution than the dusty protostellar core stage, this difference implies that Sgr B2 M is older than Sgr B2 N and the distributed protostar population. By contrast, along the Sgr B2 DS ridge, there are no H II regions, but there are ~ 100 high-mass protostars, which implies that these protostars began their formation nearly simultaneously.

The relative ages of M and the rest of the region suggest two possibilities for their formation history. If we take the ages at face value, Sgr B2 M must have collapsed first to form stars in an early event, then sometime later the DS ridge collapsed to form stars in a later event. A second possibility is that the overall collapse of both Sgr B2 M and DS began at the same time, but the Sgr B2 M region was denser and therefore had a shorter collapse time. Our catalog does not allow us to distinguish these possibilities. However, the latter scenario would predict that the cloud should be in a state of global collapse, with the least dense regions collapsing most slowly. This collapse may leave detectable kinematic signatures in the dense gas.

5. CONCLUSIONS

We have reported the detection of 243 3 mm point sources in the extended Sgr B2 cloud and determined that the majority are high-mass protostellar cores. This survey represents the first large population of protostars detected in the Galactic center and represents the largest sample yet reported of high-mass protostars.

The large population of high-mass protostellar cores indicates that the entire Sgr B2 cloud, not just the well-known clusters N, M, and S, is undergoing a burst of

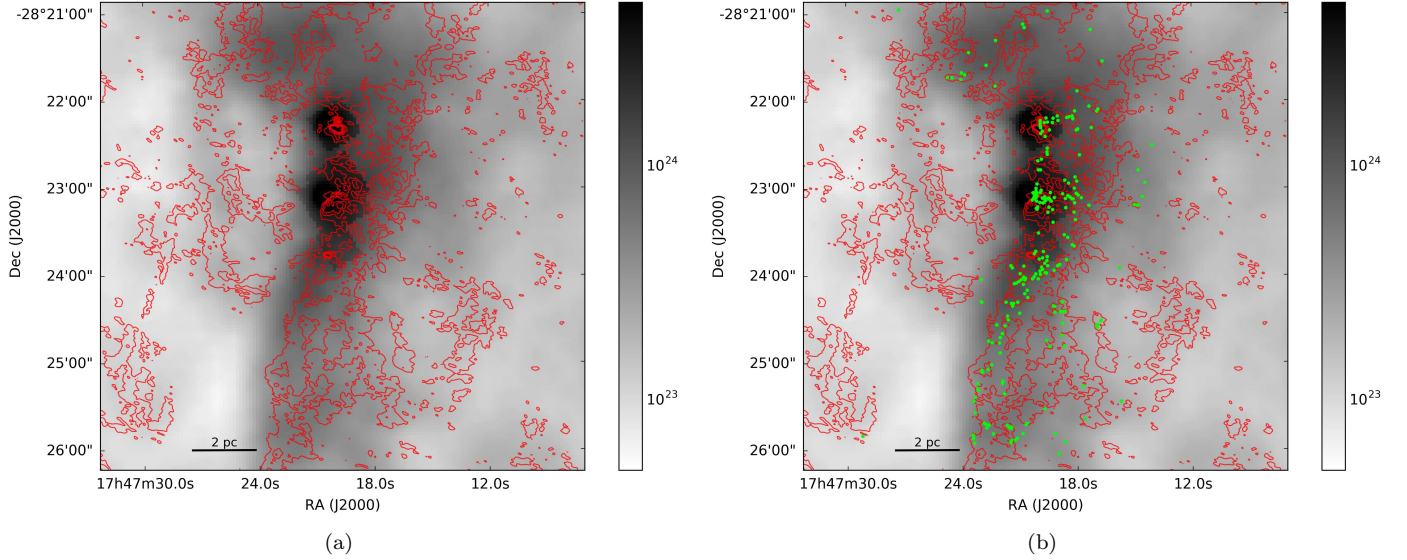


Figure 14. ALMA HC_3N peak intensity contours (red) overlaid on the derived SCUBA column density image using Herschel Hi-Gal interpolated temperatures. The HC_3N was shown in grayscale in Figure 6. Contours are at levels [3,7,11,15,19,23] K. The HC_3N bubble edges can be seen surrounding cavities in the SCUBA column density map on the east side of the main ridge. To the north, the HC_3N also traces bubbles, but these are less evident in this velocity-integrated view. The important feature discussed in Section 4.1 is the differing column density around each of the bubbles. The right figure has the cores overlaid as green dots.

star formation. More than half of the currently forming generation of stars is not associated with any of the clusters but is instead part of the extended burst.

Using Herschel, SCUBA, and SHARC data, we have measured a threshold for high-mass star formation analogous to that done in local clouds by Lada et al. (2010). We find that there are no high-mass protostars in gas below $N < 10^{23} \text{ cm}^{-2}$, and half are found above $N > 10^{24} \text{ cm}^{-2}$, at a resolution of $\approx 10'' = 0.4 \text{ pc}$. It is not yet clear whether there is a higher threshold for low-mass star formation, but the threshold for high-mass star for-

mation appears consistent with that theorized for Galactic plane conditions.

The large detected population of high-mass protostars implies a much larger population of as-yet undetectable lower-mass protostars. Future ALMA and JWST programs to probe this population would provide the data needed to directly compare star formation thresholds in the most intensely star-forming cloud in our Galaxy to those in nearby clouds.

Software: The software used to make this version of the paper is available from github at https://github.com/keflavich/SgrB2_ALMA_3mm_Mosaic/ with hash 5fdf6a9(2017-06-08).

REFERENCES

- Bally, J., Aguirre, J., Battersby, C., et al. 2010, ApJ, 721, 137
- Barnes, A. T., Longmore, S., Battersby, C., Bally, J., & Kruijssen, J. M. D. 2016, arXiv:1609.08478v1
- Barnes, A. T., Longmore, S. N., Battersby, C., et al. 2017, ArXiv e-prints, arXiv:1704.03572
- Battersby, C., Bally, J., & Svoboda, B. 2017, ApJ, 835, 263
- Battersby, C., Bally, J., Ginsburg, A., et al. 2011, A&A, 535, A128
- Caswell, J. L., Fuller, G. A., Green, J. A., et al. 2010, MNRAS, 404, 1029
- Chapin, E. L., Berry, D. S., Gibb, A. G., et al. 2013, MNRAS, 430, 2545
- Clauset, A., Rohilla Shalizi, C., & Newman, M. E. J. 2007, ArXiv e-prints, arXiv:0706.1062
- Condon, J. J., & Ransom, S. 2007, Essential Radio Astronomy (NRAO).
<http://www.cv.nrao.edu/course/astr534/ERA.shtml>
- de Pree, C. G., Gaume, R. A., Goss, W. M., & Claussen, M. J. 1996, ApJ, 464, 788
- de Vicente, P., Martin-Pintado, J., & Wilson, T. L. 1997, A&A, 320, 957

- Di Francesco, J., Johnstone, D., Kirk, H., MacKenzie, T., & Ledwosinska, E. 2008, ApJS, 175, 277
- Dicker, S. R., Mason, B. S., Korngut, P. M., et al. 2009, ApJ, 705, 226
- Dowell, C. D., Lis, D. C., Serabyn, E., et al. 1999, in Astronomical Society of the Pacific Conference Series, Vol. 186, The Central Parsecs of the Galaxy, ed. H. Falcke, A. Cotera, W. J. Duschl, F. Melia, & M. J. Rieke, 453
- Furlan, E., Fischer, W. J., Ali, B., et al. 2016, ApJS, 224, 5
- Gaume, R. A., Claussen, M. J., de Pree, C. G., Goss, W. M., & Mehringer, D. M. 1995, ApJ, 449, 663
- Ginsburg, A., Glenn, J., Rosolowsky, E., et al. 2013, ApJS, 208, 14
- Ginsburg, A., Walsh, A., Henkel, C., et al. 2015, A&A, 584, L7
- Ginsburg, A., Henkel, C., Ao, Y., et al. 2016, A&A, 586, A50
- Hasegawa, T., Sato, F., Whiteoak, J. B., & Miyawaki, R. 1994, ApJL, 429, L77
- Henshaw, J. D., Longmore, S. N., Kruijssen, J. M. D., et al. 2016, MNRAS, 457, 2675
- Immer, K., Kauffmann, J., Pillai, T., Ginsburg, A., & Menten, K. M. 2016, A&A, 595, A94
- Johnston, K. G., Beuther, H., Linz, H., et al. 2014, A&A, 568, A56
- Kauffmann, J., Bertoldi, F., Bourke, T. L., Evans, II, N. J., & Lee, C. W. 2008, A&A, 487, 993
- Kauffmann, J., Pillai, T., Zhang, Q., et al. 2016a, ArXiv e-prints, arXiv:1610.03499
- . 2016b, ArXiv e-prints, arXiv:1610.03502
- Kroupa, P. 2001, MNRAS, 322, 231
- Kruijssen, J. M. D., Dale, J. E., & Longmore, S. N. 2015, MNRAS, 447, 1059
- Krumholz, M. R., & McKee, C. F. 2008, Nature, 451, 1082
- Lada, C. J., Lombardi, M., & Alves, J. F. 2010, ApJ, 724, 687
- Longmore, S. N., Kruijssen, J. M. D., Bally, J., et al. 2013, MNRAS, 433, L15
- Martín-Pintado, J., Gaume, R. A., Rodríguez-Fernández, N., de Vicente, P., & Wilson, T. L. 1999, ApJ, 519, 667
- Mason, B. D., Hartkopf, W. I., Gies, D. R., Henry, T. J., & Helsel, J. W. 2009, AJ, 137, 3358
- Mehringer, D. M., de Pree, C. G., Gaume, R. A., Goss, W. M., & Claussen, M. J. 1995, ApJL, 442, L29
- Mehringer, D. M., & Menten, K. M. 1997, ApJ, 474, 346
- Molinari, S., Swinyard, B., Bally, J., et al. 2010, A&A, 518, L100
- Molinari, S., Schisano, E., Elia, D., et al. 2016, A&A, 591, A149
- Muno, M. P., Bauer, F. E., Baganoff, F. K., et al. 2009, ApJS, 181, 110
- Ossenkopf, V., & Henning, T. 1994, A&A, 291, 943
- Ossenkopf-Okada, V., Csengeri, T., Schneider, N., Federrath, C., & Klessen, R. S. 2016, A&A, 590, A104
- Pierce-Price, D., Richer, J. S., Greaves, J. S., et al. 2000, ApJL, 545, L121
- Pree, C. G. D., Peters, T., Low, M. M. M., et al. 2015, arXiv:1511.05131v1
- Rathborne, J. M., Longmore, S. N., Jackson, J. M., et al. 2015, ApJ, 802, 125
- Reid, M. J., Menten, K. M., Zheng, X. W., Brunthaler, A., & Xu, Y. 2009, ApJ, 705, 1548
- Sadavoy, S. I., Stutz, A., Schnee, S., et al. 2016, arXiv:1601.06769v1
- Sahai, R., Güsten, R., & Morris, M. R. 2012a, ApJL, 761, L21
- Sahai, R., Morris, M. R., & Claussen, M. J. 2012b, ApJ, 751, 69
- Sanchez-Monge, A., Schilke, P., Schmiedeke, A., et al. 2017, ArXiv e-prints, arXiv:1704.01805
- Sato, F., Hasegawa, T., Whiteoak, J. B., & Miyawaki, R. 2000, ApJ, 535, 857
- Schmiedeke, A., Schilke, P., Möller, T., et al. 2016, A&A, 588, A143
- Schnee, S., Enoch, M., Noriega-Crespo, A., et al. 2010, ApJ, 708, 127
- Shetty, R., Beaumont, C. N., Burton, M. G., Kelly, B. C., & Klessen, R. S. 2012, MNRAS, 425, 720
- Shirley, Y. L., Mason, B. S., Mangum, J. G., et al. 2011, AJ, 141, 39
- Stanimirovic, S. 2002, in Astronomical Society of the Pacific Conference Series, Vol. 278, Single-Dish Radio Astronomy: Techniques and Applications, ed. S. Stanimirovic, D. Altschuler, P. Goldsmith, & C. Salter, 375–396
- Wenger, M., Ochsenbein, F., Egret, D., et al. 2000, A&AS, 143, 9
- Yusef-Zadeh, F., Hewitt, J. W., & Cotton, W. 2004, ApJS, 155, 421

APPENDIX

A. SINGLE DISH COMBINATION

To measure the column density at a resolution similar to Lada et al. (2010), we needed to use ground-based single-dish data with resolution $\sim 10''$. We combined these images with Herschel data, which recover all angular scales, to fill in the missing ‘short spacings’ from the ground-based data.

Specifically, we combine the SHARC 350 μm (Dowell et al. 1999) and SCUBA 450 μm (Pierce-Price et al. 2000; Di Francesco et al. 2008) with Herschel 350 and 500 μm data (Molinari et al. 2016), respectively.

Combining single-dish with ‘interferometer’ data, or data that are otherwise insensitive to large angular scales, is not a trivial process. The standard approach advocated by the ALMA project is to use the ‘feather’ process, in which two images are Fourier-transformed, multiplied by a weighting function, added together, and Fourier transformed back to image space (see equations in §5.2 of Stanimirovic 2002). This process is subject to substantial uncertainties, particularly in the choice of the weighting function.

Two factors need to be specified for linear combination: the beam size of the ‘single-dish’, or total power, image, and the largest angular scale of the ‘interferometer’ or filtered image. While the beam size is sometimes well-known, for single dishes operating at the top of their usable frequency range (e.g., the CSO at 350 μm or GBT at 3 mm), there are uncertainties in the beam shape and area and there are often substantial sidelobes. In interferometric data, the largest angular scale is well-defined in the originally sampled UV data, but is less well-defined in the final image because different weighting factors change the recovered largest angular scale. For ground-based filtered data, the largest recoverable angular scale is difficult to determine and requires concerted effort (e.g., Ginsburg et al. 2013; Chapin et al. 2013).

To assess the uncertainties in image combination, particularly on the brightness distribution (e.g. Ossenkopf-Okada et al. 2016), we have performed a series of experiments combining the Herschel with the SCUBA data using different weights applied to the SCUBA data. As discussed in Section 2, we empirically determined the scale factor required for the best match between SCUBA and Herschel data was $3\times$, which is shockingly large but justifiable. In the experiment shown in Figure 15, we show the images and resulting histograms when we combine the Herschel data with the SCUBA data scaled by a range of factors from $0.5\times$ to $10\times$. The changes to the high end of the histogram are dramatic, but the middle region containing most of the pixels (and most relevant to the discussion of thresholds in the paper) is hardly affected. Additionally, we show the cumulative distribution function of core background surface brightnesses (as in Figure 10), showing again that only the high end is affected.

B. SELF-CALIBRATION

We demonstrate the impact of self-calibration in this section. The adopted approach used three iterations of phase-only self-calibration followed by two iterations of phase and amplitude self-calibration. Each iteration involved slightly different imaging parameters. The final, deepest clean used a threshold mask on the previous shallower clean. The script used to produce the final images is available at https://github.com/keflavich/SgrB2_ALMA_3mm_Mosaic/blob/5fdf6a9/script_merge/selfcal_continuum_merge_7m.py. The effects are shown with a cutout centered on the most affected region around Sgr B2 M in Figure 16.

C. PHOTOMETRIC CATALOG

We include the full catalog here. Table ?? shows the brightest 35 sources; the rest are included in a digital-only catalog. Sources are labeled based on an arbitrary source number plus any pre-existing catalog name. If a source is associated with a cluster, it has an entry corresponding to that cluster in the `Cluster` column; association is determined by checking whether a source is within a particular distance of the cluster center as defined by Schmiedeke et al. (2016). A source `Classification` column is included, which states whether the source is a strong or weak detection, whether it has an X-ray association, whether it has a maser association, and its SIMBAD classification if it has one. Measurements reported include the peak flux density $S_{\nu,\max}$, the corresponding brightness temperature $T_{B,\max}$, the integrated flux density within a beam ($0.5''$) radius, the background RMS flux level σ_{bg} as an estimate of the local noise, the spectral index α and the error on that $E(\alpha)$. Mass and column density estimates are given for an assumed temperature $T = 40$ K (M_{40K} and $N(\text{H}_2)_{40K}$); for sources with $T_{B,\max} \gtrsim 20$ K, these estimates are unlikely to be useful since the assumed temperature is likely to be much lower than the true temperature. For sources with $T_{B,\max} > 40$ K, it is not possible to measure a mass assuming $T = 40$ K.

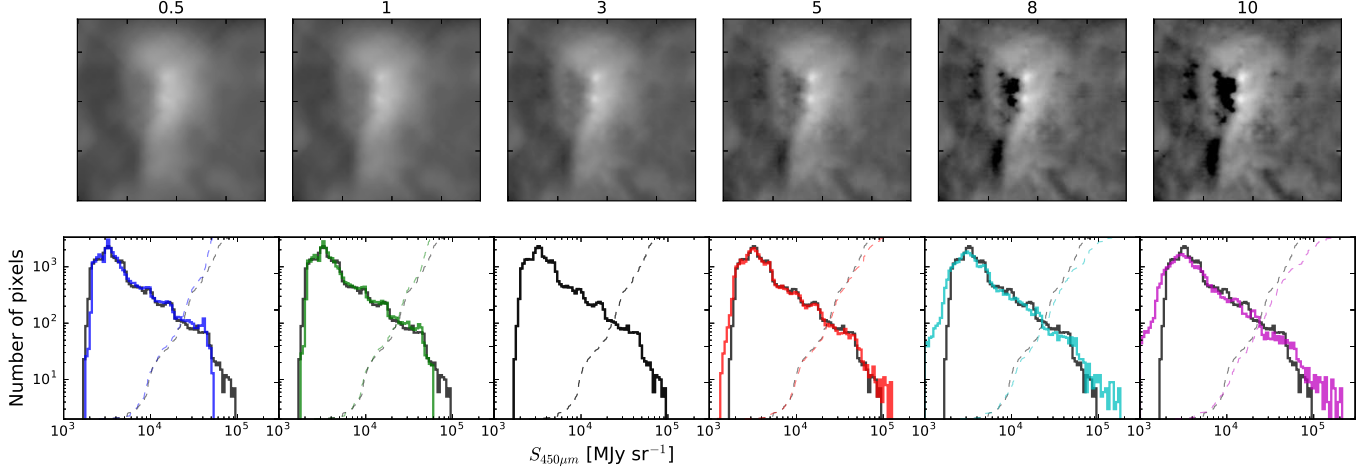


Figure 15. A demonstration of the effects of using different calibration factors when combining the SCUBA data with the Herschel data using the ‘feather’ process. The numbers above each panel show the scale factor applied to the SCUBA data before fourier-combining it with the Herschel data. The factor of 3 was used in this paper and shows the most reasonable balance between the high-resolution of the SCUBA data and the all-positive Herschel data. In the lower panels, the fiducial scale factor of 3 is shown in black in all panels. The solid lines show histograms of the images displayed in the top panels. The dashed lines show the cumulative distribution of the background surface brightnesses of the point sources in this sample; they are similar to the distributions shown in Figure 10.

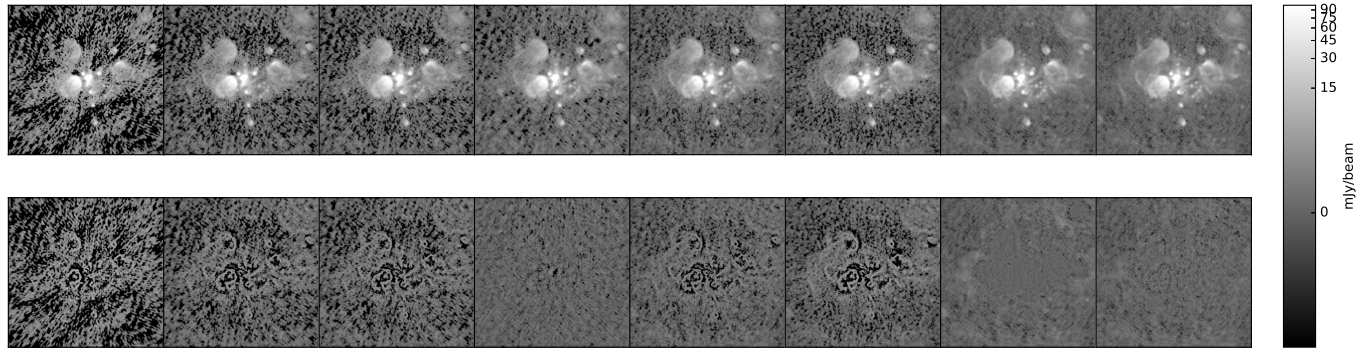


Figure 16. Progression of the self-calibration iterations. The images show, from left to right, the initial image, one, two, and three iterations of phase-only self calibration, one iteration of phase and amplitude self-calibration, one iteration of phase and amplitude self-calibration, a reimaging of the 5th iteration with a deeper 0.1 mJy threshold using a mask at the 2.5 mJy level, and finally, a sixth iteration of phase and amplitude self-cal cleaned to 0.1 mJy over a region thresholded at 1.5 mJy. All imaging was done using two Taylor terms and multiscale clean. The second row shows the corresponding residual images.

Table 3. Continuum Source IDs and photometry

ID	Cluster	Classification	Coordinates	$S_{\nu,max}$	$T_{B,max}$	$S_{\nu,tot}$	σ_{bg}	α	$E(\alpha)$	M_{40K}	$N(\text{H}_2)_{40K}$
				mJy bm^{-1}	K	mJy	mJy bm^{-1}			M_\odot	cm $^{-2}$
174 f3	M	SX_ HII	17:47:20.167 -28:23:04.809	1600	860	2400	46	0.89	0.002	-	-
234 f4	M	SX_ HII	17:47:20.214 -28:23:04.379	1100	570	900	23	0.83	0.001	-	-
176 f1	M	SX_ denseCore	17:47:20.127 -28:23:04.082	920	480	1400	30	1.2	0.006	-	-
236 f10.303	M	S_ HII	17:47:20.106 -28:23:03.729	890	460	800	19	1.1	0.015	-	-
235 f2	M	S_ HII	17:47:20.166 -28:23:03.714	820	430	670	33	1.3	0.002	-	-
172 K2	N	S_ denseCore	17:47:19.869 -28:22:18.466	370	200	650	49	2.5	0.018	-	-
175 G	M	S_ HII	17:47:20.285 -28:23:03.162	340	180	390	5.6	0.68	0.03	-	-
237 G10.44	M	S_ HII	17:47:20.241 -28:23:03.387	280	140	160	15	0.69	0.006	-	-
178 f10.37	M	SX_ HII	17:47:20.178 -28:23:06	200	100	270	18	1.5	0.039	-	-
171 K3	N	S_ HII	17:47:19.895 -28:22:17.221	190	97	280	25	1.4	0.023	-	-
177 B	M	S_M HII	17:47:19.918 -28:23:03.039	150	77	240	3.9	0.47	0.011	-	-
241	M	S_ denseCore	17:47:20.106 -28:23:03.066	140	73	120	15	1.4	0.05	-	-
179 f10.38	M	SX_ HII	17:47:20.193 -28:23:06.673	130	66	180	9.3	1.6	0.013	-	-
180 E	M	S_ HII	17:47:20.108 -28:23:08.894	130	66	190	4	0.38	0.014	-	-
173 K1	N	S_ HII	17:47:19.78 -28:22:20.743	92	48	150	4.4	0.58	0.034	-	-
170	N	S_ PartofCloud	17:47:19.895 -28:22:13.621	92	48	160	23	1.7	0.082	-	-
225 f10.33b	M	SX_ denseCore	17:47:20.116 -28:23:06.374	69	36	100	14	1.9	0.21	1200	3.6×10^{26}
96 Z10.24	-	S_M Maser	17:47:20.039 -28:22:41.25	64	33	75	1.5	0.68	0.37	1100	2.5×10^{26}
181 D	M	S_M HII	17:47:20.051 -28:23:12.91	59	31	94	1.3	0.64	0.088	990	2×10^{26}
240 f10.44b	M	SX_ HII	17:47:20.252 -28:23:06.463	57	30	51	11	1.8	0.015	960	1.8×10^{26}
233 f10.27b	M	SX_ HII	17:47:20.077 -28:23:05.383	50	26	78	18	2.3	0.18	840	1.4×10^{26}
239	M	SX_ denseCore	17:47:20.242 -28:23:07.222	45	24	46	8.6	2.3	0.091	760	1.1×10^{26}
242	M	S_ denseCore	17:47:20.129 -28:23:02.247	32	17	63	8.5	2.2	0.099	540	6.8×10^{25}
92 I10.52	M	S_ HII	17:47:20.324 -28:23:08.2	32	17	45	5.3	0.63	0.061	530	6.6×10^{25}
109	N	S_ -	17:47:19.901 -28:22:15.54	24	13	41	13	3.6	0.3	410	4.7×10^{25}
87 B9.99	M	S_ HII	17:47:19.798 -28:23:06.942	23	12	37	1.9	0.89	0.042	390	4.4×10^{25}
88	M	S_ -	17:47:19.617 -28:23:08.26	23	12	34	2.9	3.1	0.18	380	4.3×10^{25}
151 B10.06	M	S_M HII	17:47:19.86 -28:23:01.5	21	11	31	1.3	0.19	0.79	350	3.8×10^{25}
98	-	S_M Maser	17:47:19.53 -28:22:32.55	18	9.5	29	0.36	3.2	1.1	300	3.3×10^{25}
152 f10.32	M	S_ HII	17:47:20.128 -28:23:00.22	16	8.5	27	3	-0.3	0.26	270	2.9×10^{25}
86 B9.96	M	S_ HII	17:47:19.766 -28:23:10.183	16	8.3	24	1.8	1	0.089	270	2.9×10^{25}
76	S	S_ -	17:47:19.986 -28:23:48.86	15	7.9	21	0.94	3.3	0.35	250	2.7×10^{25}
97	-	S_ -	17:47:19.838 -28:22:40.07	13	6.8	20	1.1	3	0.57	220	2.3×10^{25}
85	-	S_ -	17:47:18.029 -28:23:03.61	13	6.7	14	0.17	3	0.32	210	2.2×10^{25}

The Classification column consists of three letter codes as described in Section 3.2. In column 1, S indicates a strong source, W indicates weak or low-confidence source. In column 2, an X indicates a match with the [Muno et al. \(2009\)](#) Chandra X-ray source catalog, while an underscore indicates there was no match. In column 3, M indicates a match with the, [Caswell et al. \(2010\)](#) Methanol Multibeam Survey CH₃OH maser catalog, while an underscore indicates there was no match. Finally, we include the SIMBAD ([Wenger et al. 2000](#)) source object type classification if one was found.